Journal of Materials Chemistry A

PAPER



Cite this: *J. Mater. Chem. A*, 2023, **11**, 15211

# Dynamic compensation of MnOOH to mitigate the irregular dissolution of $MnO_2$ in rechargeable aqueous $Zn/MnO_2$ batteries†

Guojun Lai,‡[a] Pengchao Ruan,‡[a] Xueting Hu,[a] Bingan Lu,[b] Shuqiang Liang,[a] Yan Tang*[a] and Jiang Zhou*[a]

Received 12th April 2023
Accepted 19th June 2023

DOI: 10.1039/d3ta02202a

rsc.li/materials-a

As a recognized promising cathode material for rechargeable aqueous Zn batteries, an $MnO_2$ cathode often suffers from rapid fading of capacity due to irreversible Mn dissolution, which hinders high-performance Zn batteries. Herein, we introduced $Ce(SO_4)_2$ additives into the electrolyte of $Zn/MnO_2$ batteries to cope with the irreversible dissolution of $MnO_2$. During charging, the MnOOH formed by the reaction between $Ce^{4+}$ and $Mn^{2+}$ deposited on the cathode with the attraction of $H^+$ and was converted subsequently to $MnO_2$ to achieve dynamic compensation. Meanwhile, MnOOH was generated from the transformation of $MnO_2$ during discharge, and the reaction between $Ce^{3+}$ and MnOOH was beneficial for the reversibility of $Ce^{4+}$, but also competitive with the disproportionation of MnOOH. As a result, $Zn/MnO_2$ batteries with $Ce(SO_4)_2$ additives showed high capacity retention of 97.4% at 1.0 A $g^{-1}$ after 1000 cycles, which far exceeded that of the batteries without $Ce(SO_4)_2$ (40.5%).



[a]*School of Materials Science and Engineering, Hunan Provincial Key Laboratory of Electronic Packaging and Advanced Functional Materials, Central South University, Changsha 410083, China. E-mail: ty_csu@csu.edu.cn; zhou_jiang@csu.edu.cn*

[b]*School of Physics and Electronics, Hunan University, Changsha 410082, China*

† Electronic supplementary information (ESI) available. See DOI: https://doi.org/10.1039/d3ta02202a

‡ These authors contributed equally to the work.

*Professor Jiang Zhou received a bachelor's degree (2011) and doctorate (2015) from Central South University (CSU). He studied in the research team of Professor Hua Zhang at Nanyang Technological University as an exchange doctoral student. He has carried out postdoctoral research in the research team of Professor Ju Li at the Massachusetts Institute of Technology since 2016. He joined CSU as a professor at the end of 2017. His research interests include lithium (sodium)-ion batteries and aqueous zinc-ion batteries. He has published more than 100 articles in international journals, which has attracted more than 18000 citations with an h-index of 71. He has been ranked by Web of Science (Clarivate) as a "highly cited researcher" since 2021.*

## 1 Introduction

Rechargeable aqueous zinc batteries (RAZBs) have attracted great interest in the energy-storage market due to their prominent strengths: plentiful resource of Zn, high theoretical capacity of the zinc anode, and high safety.[1–3] The cathode plays an important part in battery performance. The cathode materials of RAZBs are based mainly on Mn and V, organic compounds, and Prussian blue analogs. $MnO_2$ is an extensively applied cathode material due to high theoretical capacity and affordable cost.[4–7] Recently, substantial studies on the $MnO_2$ cathode have been conducted to raise the electrochemical performance and have made great strides. However, the cycle stabilities remain unsatisfactory, which is caused by the irreversible dissolution of $MnO_2$.[8] The reduced utilization rate of the active materials is caused by the dissolution of cathode materials, and the possibility of unfavorable side effects on the electrode interface will be increased. Simultaneously, structural degradation and performance attenuation are induced.[9]

Various strategies have been postulated to solve these issues, including electrolyte additives (*e.g.*, $Mn^{2+}$) and modification of electrode interfaces (inorganic/organic coatings).[10–12] To achieve $Mn^{2+}$ equilibrium in an electrolyte, $MnSO_4$ was introduced into the $ZnSO_4$ electrolyte to restrain dissolution of the $MnO_2$ cathode.[10] Also, "graphene scrolls" can be used as a protector, which inhibits the dissolution of $MnO_2$ effectively and enhances conductivity.[11] For the $Zn/MnO_2$ battery, the structural transformation of $MnO_2$ during cycling will likely be responsible for the instability of $MnO_2$, which promotes the dissolution of $MnO_2$. Moreover, during discharging/charging, $MnO_2$ is reduced to $Mn^{2+}$ and $Mn^{3+}$, and the disproportionation reaction of $Mn^{3+}$ (which helps to enhance of $Mn^{2+}$) will promote dissolution further.[12,13] Introduction of a certain amount of $Mn(CF_3SO_3)_2$ to $Zn(CF_3SO_3)_2$ will lead to inhibition of the unfavorable dissolution of $Mn^{2+}$, with *in situ* generation of a uniform porous $MnO_x$ layer. The latter will deposit on the cathode and have a significant role in maintaining the integrity of the $MnO_2$ cathode.[14] Hence, such *in situ* generation could be a tactic to alleviate the dissolution of $MnO_2$. Inspired by the mechanism of $MnO_2$ dissolution and the concept of *in situ* generation, we postulated a scheme whereby MnOOH was generated *in situ* in the electrolyte and deposited on the $MnO_2$ cathode and "dynamic compensation" occurred.

Herein, we introduced $Ce(SO_4)_2$ as an additive of the basic electrolyte (2 M $ZnSO_4$ + 0.1 M $MnSO_4$) for a Zn/$MnO_2$ battery, which was noted as a Zn–Ce electrolyte. In the basic electrolyte, the $Mn^{2+}$ generated from the disproportionation with MnOOH in discharging is regarded to dissolve in the electrolyte, which cannot take advantage of the $MnO_2$ cathode. While the introduced $Ce^{4+}$ reacted with $Mn^{2+}$ can make a contribution to the conversion of $Mn^{2+}$ to MnOOH, and the generated MnOOH deposits partly on the cathode due to the attraction of $H^+$ formed during charging. The part of MnOOH that transforms to $MnO_2$ during charging compensates for the active substance to achieve dynamic compensation. Meanwhile, MnOOH is generated from the transformation of $MnO_2$ during discharging. The reaction between $Ce^{3+}$ and MnOOH is beneficial for the reversibility of $Ce^{4+}$, but also competes with the disproportionation of MnOOH. As a result, compared with the basic electrolyte, the Zn/$MnO_2$ battery with a Zn–Ce electrolyte shows an excellent cycle life and capacity retention (97.4% *vs.* 40.5% at 1.0 A $g^{-1}$ after 1000 cycles).

## 2 Results and discussion

Visualization of the mechanism of dynamic compensation was investigated through a series of demonstrations conducted on $MnO_2$ cathodes and electrolytes at different charge/discharge states (Fig. 1). The conversion of $MnO_2$ was found to be related with eqn (1) (Fig. 1a).[10,15] According to the results of *ex situ* X-ray diffraction (XRD), MnOOH was transformed from $MnO_2$ during discharging and the opposite reaction occurred during charging. However, during discharging, parts of MnOOH tended to transform into $Mn^{2+}$ *via* disproportionation, and this phenomenon was consistent with increases in levels of Mn-$OSO_3^{2-}$ and Mn in the electrolyte (Fig. 1b and S1†).[16] Also, parts of $Mn^{2+}$ would diffuse into the electrolyte and could not return back to the cathode spontaneously during charging, which is responsible for the capacity fading of $MnO_2$.

$$H^+ + e^- + MnO_2 \leftrightarrow MnOOH \quad (1)$$

For the Zn–Ce electrolyte, the increasing diffraction peaks of MnOOH on the cathode and decreasing peaks of Mn-$OSO_3^{2-}$ in the electrolyte were found during charging, which was not in accordance with eqn (1) (Fig. 1c and d). Addition of $Ce(SO_4)_2$ was considered to be the reason for this deviation, which was investigated further by ultraviolet-visible (UV-vis) spectroscopy. As shown in UV-vis and Raman spectra, periodic oscillation could be found for $Ce^{3+}$ and $Ce^{4+}$ (Fig. 1e and f).[17,18] Based on these analytical results, the role of $Ce^{4+}$ could be proposed as shown in eqn (2). With respect to the reaction, addition of $Ce^{4+}$ is related to the redox couple for $Mn^{2+}$. As mentioned above, the MnOOH generated during discharging tends to be converted to $Mn^{2+}$ with the Jahn–Teller effect. During charging, parts of $Mn^{2+}$ cannot return back to $MnO_2$. $Ce^{4+}$ can react with $Mn^{2+}$ to form MnOOH *via* a redox reaction during charging. Subsequently, parts of MnOOH will deposit on the cathode by $H^+$ attraction and transform further to $MnO_2$ for participation in the electrochemical reaction on the cathode, which helps to increase the mass of active substances and enhance the capacity (Fig. 1c and S2†).

$$Mn^{2+} + Ce^{4+} + 2H_2O \leftrightarrow MnOOH + Ce^{3+} + 3H^+ \quad (2)$$

Furthermore, the Zn–Ce electrolyte was centrifugated and analyzed (Fig. 2). The peaks located at 882.6/886.6 eV and 883.0 eV in the high-resolution XPS Ce 3d spectrum for the Zn–Ce electrolyte represented $Ce^{4+}$ and $Ce^{3+}$, respectively. The peaks located at 642.5/653.9 eV and 643.1/655.0 eV in the high-resolution XPS Mn 2p spectrum for the sediment represent $Mn^{3+}$ and $Mn^{2+}$, respectively (Fig. 2a).[19–23] Furthermore, the lattice-oxygen Mn–O–Mn and surface-adsorbed oxygen Mn–O–H also confirmed the generation of MnOOH.[24] The XRD pattern showed that the sediment was mainly MnOOH (space group: *Pbnm*, JCPDS card number: 01-089-2354) (Fig. 2b). Moreover, the obvious co-existing signals of $Ce^{4+}$ and $Ce^{3+}$ demonstrated the reversibility of the $Ce^{4+}/Ce^{3+}$ conversion reaction (Fig. 2c). Combined with the oscillation of $Ce^{3+}/Ce^{4+}$ and $Mn^{2+}$/MnOOH, we speculated that eqn (2) was reversible. That is, the decline of $Ce^{3+}$ upon discharge was related to negative eqn (2), consistent with the increase in $Ce^{4+}$ and $Mn^{2+}$ (Fig. 1d and f). Moreover, the increase in $Ce^{4+}$ and decrease in $Ce^{3+}$ were shown by UV-vis spectroscopy, which was related to the reaction between $Ce^{3+}$ and MnOOH during discharge (Fig. 1e). During discharge, the reaction between $Ce^{3+}$ and MnOOH would be competitive, with the disproportionation of MnOOH, which would be beneficial for the $Ce^{4+}/Ce^{3+}$ reversible conversion reaction, and the opposite process would be found simultaneously. Herein, Hess's law can be introduced to explain this phenomenon (see ESI Discussion†). The change in $Mn^{2+}$ and MnOOH with eqn (1) is the driving force of eqn (2). Based on this interpretation, the assumption that positive eqn (2) is influenced by the peak content of $Mn^{2+}$ in the electrolyte at the termination of discharge is reasonable. The Mn content stayed about the same after one cycle because the balance of $Ce^{4+}/Ce^{3+}$ is obtained and negative eqn (2) competes with the disproportionation of MnOOH (Fig. S1†). As a result, stronger peaks of MnOOH can be found after 10 cycles, which is caused by the addition of $Ce^{4+}$ (Fig. S3†). At the beginning of the cycle, positive eqn (2) is stronger due to the amount of $Ce^{4+}$, whereas the balance is built later (Fig. 2c). Moreover, the variation in Mn at the cathode was studied by X-ray fluorescence (XRF) spectrometry (Fig. S4†). The

 

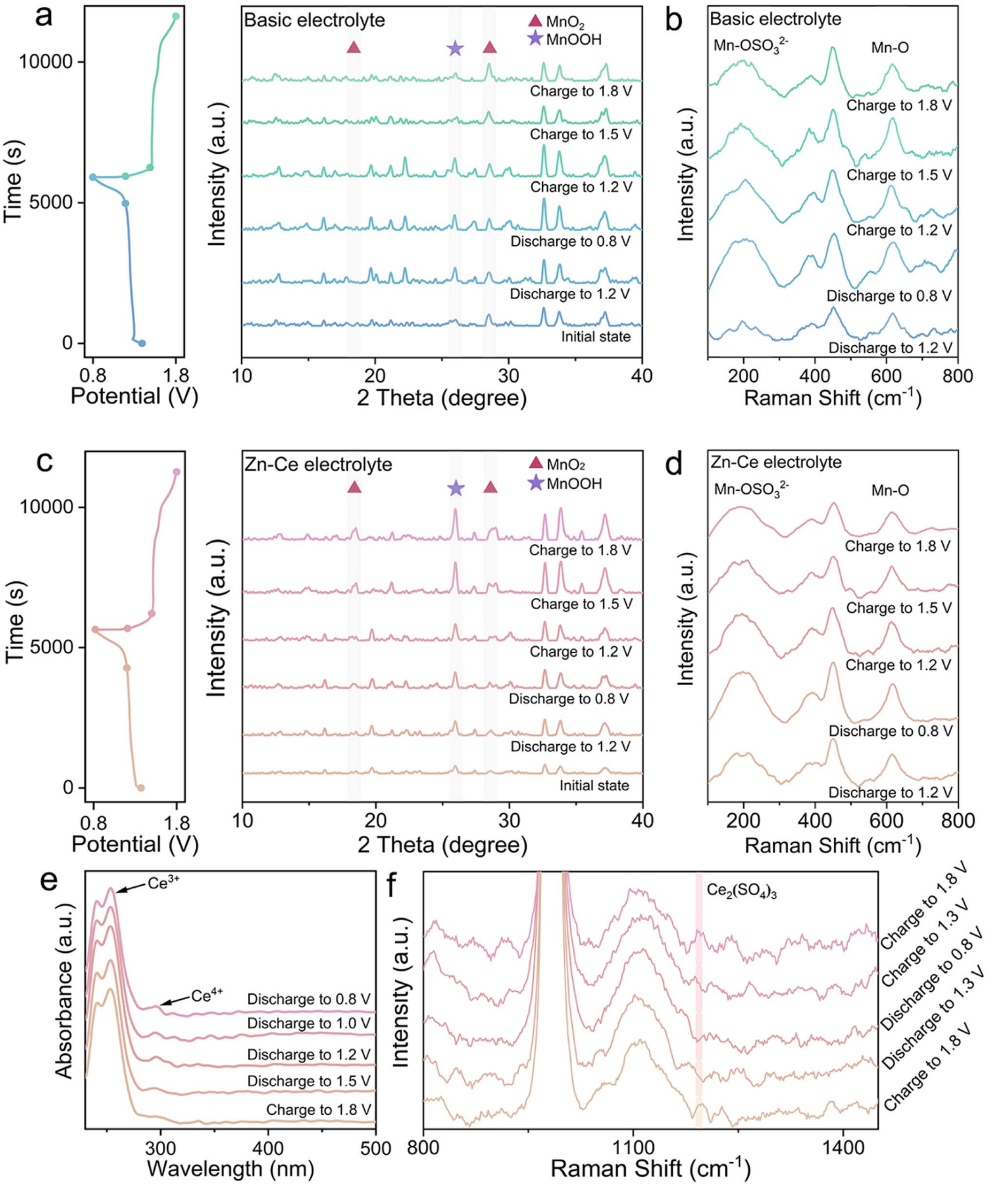


Fig. 1 Investigation of the dynamic compensation mechanism. *Ex situ* (a) XRD patterns for the $MnO_2$ cathodes and (b) Raman spectra for the electrolyte of the Zn/$MnO_2$ battery with the basic electrolyte at different charge/discharge stages. *Ex situ* (c) XRD patterns for $MnO_2$ cathodes and (d) Raman spectra for the electrolyte of the Zn/$MnO_2$ battery with the Zn–Ce electrolyte at different charge/discharge stages. (e) UV-vis spectroscopy and (f) Raman spectra of the Zn–Ce electrolyte at different charge/discharge stages.

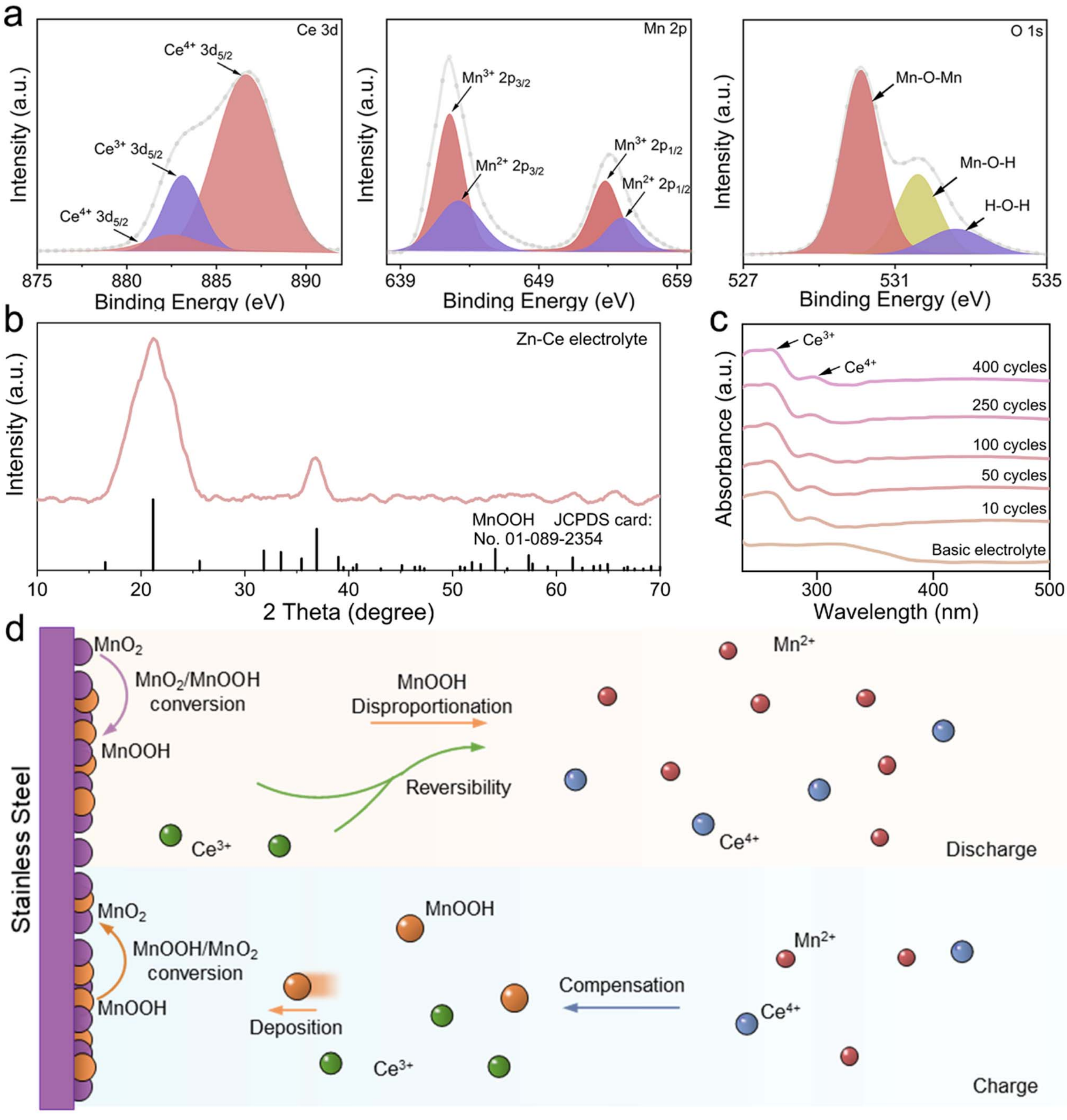


Fig. 2 Characterization of the results in the Zn–Ce electrolyte. (a) High-resolution X-ray photoelectron spectroscopy (XPS) of Ce 3d, Mn 2p, and O 1s of the Zn–Ce electrolyte. (b) XRD pattern of the sediment in the Zn–Ce electrolyte. (c) UV-vis spectroscopy of the Zn–Ce electrolyte in different cycles. (d) Dynamic compensation mechanism for the Zn/$MnO_2$ battery with the Zn–Ce electrolyte (schematic).

mass of Mn was ∼45% after 50 cycles compared with the first cycle in the basic electrolyte, whereas it was 84% in the Zn–Ce electrolyte, showing that the dynamic compensation mechanism could inhibit the dissolution of Mn effectively. In summary, $Mn^{2+}$ generated from the disproportionation of MnOOH during discharge was reconverted to MnOOH with the addition of $Ce^{4+}$ during charging. MnOOH would deposit on the cathode by $H^+$ attraction and be converted to $MnO_2$ for capacity compensation during charging. Meanwhile, during discharge, $Ce^{3+}$ would react with MnOOH and be converted to $Ce^{4+}$ to achieve dynamic reversible $Ce^{4+}/Ce^{3+}$ conversion (Fig. 2d).

The scanning electron microscope (SEM) images, corresponding mapping images, and energy dispersive spectroscopy (EDS) of $MnO_2$ cathodes upon discharging to 0.8 V and charging to 1.8 V revealed that the structures of $MnO_2$ in the two types of electrolytes were distinct (Fig. S5–S7†). The concentration of Zn, O, and S suggested that $Zn_4SO_4(OH)_6 \cdot 4H_2O$ appeared on the $MnO_2$ cathode in the basic electrolyte (Fig. S6†).[25] During discharge, the increasing $OH^-$ in the electrolyte was the result of positive eqn (1), and reacted with $Zn^{2+}$ and $SO_4^{2-}$ on the cathode to form $Zn_4SO_4(OH)_6\cdot 4H_2O$, which corresponded to the cathode in the basic electrolyte (Fig. S5a†). In contrast, the cathode surface in the Zn–Ce electrolyte was mainly MnOOH instead of $Zn_4SO_4(OH)_6\cdot 4H_2O$ because $OH^-$ was likely to react with the extra $H^+$ generated in eqn (2) rather than $Zn^{2+}$ and $SO_4^{2-}$ (Fig. S7 and S8†).

Cyclic voltammetry (CV) at scan rates from 0.1 to 1 mV $s^{-1}$ was performed to investigate the electrochemistry of $Zn/MnO_2$ batteries with the Zn–Ce electrolyte (Fig. 3a). As reported previously, the scan ($\nu$) and peak current ($i$) can be used to analyze the contribution of diffusive-controlled and capacitive-controlled effects based on eqn (3) and (4).[26,27]

$$i = a\nu^b \quad (3)$$

$$\log(i) = b\log(\nu) + \log(a) \quad (4)$$

where $a$ and $b$ are adjustable parameters, $0.5 \le b \le 1$ denotes a greater diffusive-controlled contribution in the electrochemical process if $b$ is close to 0.5, and a greater capacitive-controlled contribution in the electrochemical process if $b$ approaches 1.

$$i = k_1\nu + k_2\nu^{0.5} \quad (5)$$

where $i$ is the peak current, $\nu$ is the scan rate, $k_2\nu^{0.5}$ represents the diffusive-controlled contribution, and $k_1\nu$ represents the capacitive-controlled contribution.

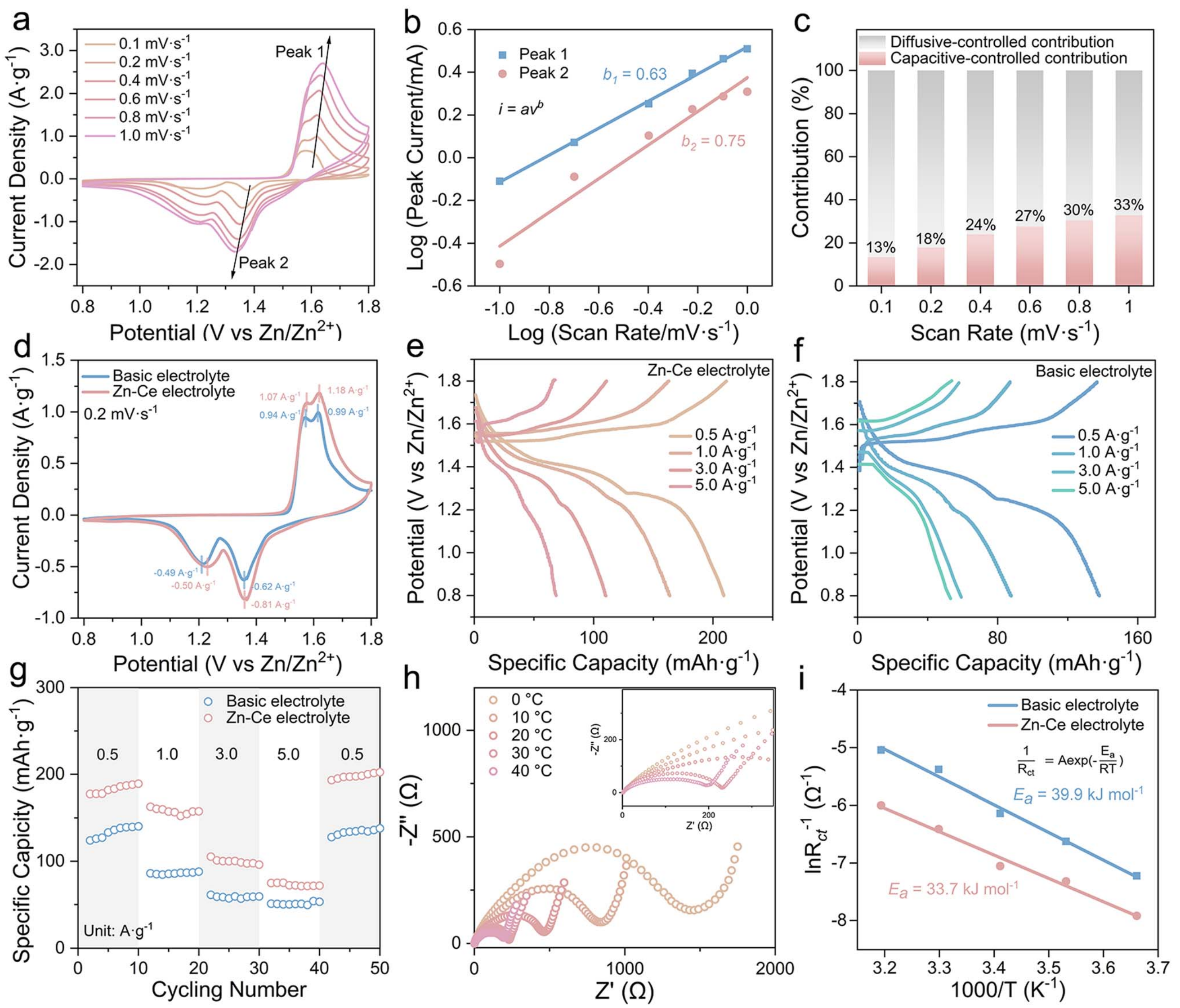


Fig. 3 Electrochemical performance of the $Zn/MnO_2$ battery. (a) CV curves at various scan rates from 0.1 to 1.0 mV $s^{-1}$, (b) relationship between log($i$) and log($\nu$) plot at corresponding redox peaks, and (c) capacitive contribution ratio of the $Zn/MnO_2$ battery with the Zn–Ce electrolyte. (d) CV curves of the $Zn/MnO_2$ battery with the Zn–Ce electrolyte and basic electrolyte at 0.2 mV $s^{-1}$. (e and f) Charge/discharge curves and (g) rate performance of $Zn/MnO_2$ batteries with the basic electrolyte and Zn–Ce electrolyte at different current densities. (h) EIS curves of $Zn/MnO_2$ batteries with the Zn–Ce electrolyte at different temperatures. (i) Activation energy ($E_a$) values of $Zn/MnO_2$ batteries with the basic electrolyte and Zn–Ce electrolyte.

The two peak-current values were utilized as the $i$ values in eqn (3) and (4), and the linear relationship between log($i$) and log($v$) is shown in Fig. 3b. The corresponding $b_1$ and $b_2$ values of peaks were 0.63 and 0.75, respectively.[28] Furthermore, the capacitive contribution ratio could be calculated using eqn (5). The result showed that the electrochemical behavior of the $Zn/MnO_2$ battery with the Zn–Ce electrolyte was dominated by a diffusive-controlled contribution (Fig. 3c).[29]

According to the CV curves at 0.2 mV $s^{-1}$ (Fig. 3d), one pair of redox peak corresponding to the $MnO_2$/MnOOH conversion reaction could be found in the $Zn/MnO_2$ battery with two types of electrolytes, which was consistent with the charge/discharge plateaus in galvanostatic charge/discharge curves (GCDs).[30–32] Meanwhile, the higher current density of $Zn/MnO_2$ batteries with $Ce(SO_4)_2$ additives in comparison with that without $Ce(SO_4)_2$ additives indicated a higher specific capacity, which was ascribed to the dynamic compensation mechanism (Fig. 3e–g).[33] Therefore, the $Zn/MnO_2$ battery with the Zn–Ce electrolyte exhibited a reversible capacity of 190.4 mA h $g^{-1}$ at 0.5 A $g^{-1}$ and maintained 105.2 mA h $g^{-1}$ at 3 A $g^{-1}$, and the capacity returned to 202.4 mA h $g^{-1}$ when the current density returned to 0.5 A $g^{-1}$ after 40 cycles, thereby demonstrating outstanding cycling stability (Fig. 3f). The charge-transfer resistance of the $Zn/MnO_2$ battery with the Zn–Ce electrolyte at 30 °C was 217 Ω, which was far lower than that of the $Zn/MnO_2$ battery with the basic electrolyte (608.6 Ω), indicating faster charge-transfer kinetics (Table S1†). Compared with the higher activation energy of the $Zn/MnO_2$ battery with the basic electrolyte (39.9 kJ $mol^{-1}$), that of the $Zn/MnO_2$ battery with Zn–Ce electrolyte was lower (33.7 kJ $mol^{-1}$), thereby indicating better reaction kinetics and resulting in a satisfactory rate performance (Fig. 3h–i and S9†). The lower $R_{ct}$ of the $Zn/MnO_2$ battery with the Zn–Ce electrolyte at different cycles was attributed to the accelerated kinetics process shown above. Furthermore, accelerated kinetics at the anode was also shown with activation energy using electrochemical impedance spectroscopy (EIS) at different temperatures (Fig. S10 and Table S2†).[30]

Fig. 4 shows a comparison of the electrochemical performance of $Zn/MnO_2$ batteries. The $R_{ct}$ changes of $Zn/MnO_2$ batteries with the basic electrolyte and Zn–Ce electrolyte were studied (Fig. 4a, S11 and S12†). With an increase in shelf time, $Zn/MnO_2$ batteries with the Zn–Ce electrolyte exhibited a much slower $R_{ct}$ growth compared with $Zn/MnO_2$ batteries with the basic electrolyte, denoting better stability for storage. Moreover, this phenomenon was confirmed by the impendence–time curves of the $Zn/MnO_2$ battery with the basic electrolyte and Zn–Ce electrolyte at 1000 Hz (Fig. S13†). Meanwhile, the $Zn/MnO_2$ battery with the Zn–Ce electrolyte delivered greater capacity retention after 200 cycles at different temperatures, indicating superior wide-temperature stability (Fig. 4b and S14†). Furthermore, benefiting from the dynamic

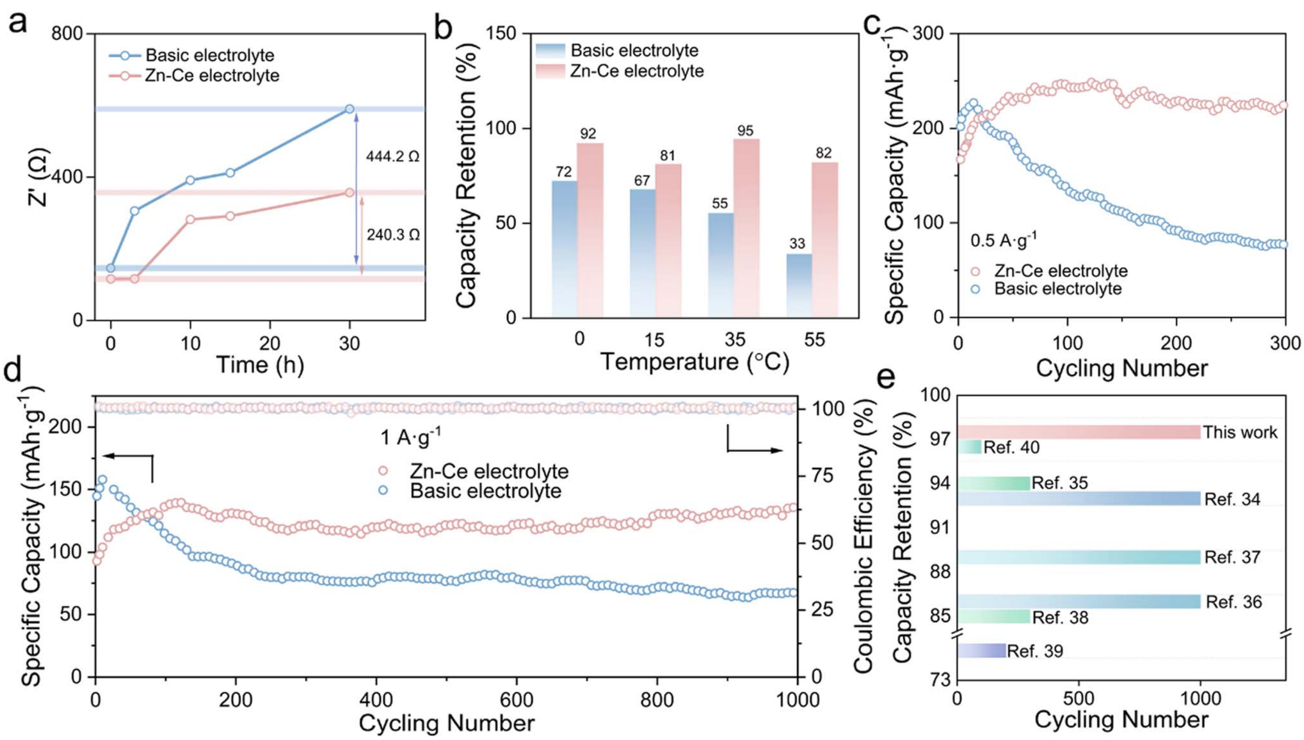


Fig. 4 Comparison of the electrochemical performance of $Zn/MnO_2$ batteries. (a) Changes in $R_{ct}$ values of $Zn/MnO_2$ batteries with the basic electrolyte and Zn–Ce electrolyte during 30 h at room temperature. (b) Capacity retention of $Zn/MnO_2$ batteries with the basic electrolyte and Zn–Ce electrolyte after 200 cycles at 0, 15, 35, and 55 °C. (c and d) Long cycling performance of $Zn/MnO_2$ batteries with the basic electrolyte and Zn–Ce electrolyte at 0.5 and 1.0 A $g^{-1}$. (e) Comparison of electrochemical performance of the $Zn/MnO_2$ battery based on the Zn–Ce electrolyte with other $Zn/MnO_2$ batteries reported previously.[34–40]

 

compensation of MnOOH, the Zn/$MnO_2$ battery with the Zn–Ce electrolyte achieved reversible capacity retention of 97.4% and a capacity of 130.1 mA h $g^{-1}$ at 1 A $g^{-1}$ after 1000 cycles (*vs.* 40.5% and 75.8 mA h $g^{-1}$ for the Zn/$MnO_2$ battery with the basic electrolyte), and identical results were obtained at a current density of 0.5 A $g^{-1}$ (Fig. 4c and d). It also had greater capacity retention compared with the partial Zn/$MnO_2$ battery based on different optimization methods (Fig. 4e and Table S3†).[34–40]

# 3 Conclusions

The Zn–Ce electrolyte was prepared to enhance the capacity retention of Zn/$MnO_2$ batteries. The dynamic compensation mechanism was proposed to mitigate the disproportionation of MnOOH. $Mn^{2+}$ formed from the disproportionation of MnOOH during discharging diffused into the electrolyte. Introduction of $Ce^{4+}$ led it to react with part of $Mn^{2+}$ to form MnOOH, which deposited partly on the cathode *via* the attraction of $H^+$, and subsequently transformed to $MnO_2$ during charging to dynamically compensate the active substance. Meanwhile, during discharge, $Ce^{3+}$ reacted with MnOOH to reversibly convert to $Ce^{4+}$, which inhibited the disproportionation of MnOOH. Benefiting from this strategy, Zn/$MnO_2$ batteries with $Ce(SO_4)_2$ additives showed a capacity retention of 97.4% at 1.0 A $g^{-1}$ after 1000 cycles, which far exceeded that of the Zn/$MnO_2$ battery without $Ce(SO_4)_2$ additives.

# Author contributions

J. Z. and Y. T. conceived and supervised the research. G. L. and P. R. carried out the experiments and analysed the experimental data. B. L., S. L., and X. H. helped with the analysis of electrochemical data. All authors commented on the manuscript.

# Conflicts of interest

There are no conflicts of interest to declare.

# Acknowledgements

This work was supported by the National Natural Science Foundation of China (52172263, 51932011), Natural Science Foundation of Hunan Province (2022JJ30051), Hunan Natural Science Fund for Distinguished Young Scholar (2021JJ10064), and Program of Youth Talent Support for Hunan Province (2020RC3011).

# Notes and references

1 Z. Xing, G. Xu, J. Han, G. Chen, B. Lu, S. Liang and J. Zhou, *Trends Chem.*, 2023, **5**, 380–392.
2 R. Yi, X. Shi, Y. Tang, Y. Yang, P. Zhou, B. Lu and J. Zhou, *Small Struct.*, 2023, 2300020.
3 W. Nie, H. Cheng, Q. Sun, S. Liang, X. Lu, B. Lu and J. Zhou, *Small Methods*, 2023, 2201572.
4 S. Chen, K. Li, K. S. Hui and J. Zhang, *Adv. Funct. Mater.*, 2020, **30**, 2003890.
5 J. Ding, Z. Du, L. Gu, B. Li, L. Wang, S. Wang, Y. Gong and S. Yang, *Adv. Mater.*, 2018, **30**, 1800762.
6 Y. Lu, T. Zhu, W. van den Bergh, M. Stefik and K. Huang, *Angew. Chem., Int. Ed.*, 2020, **59**, 17004–17011.
7 X. Chen, P. Ruan, X. Wu, S. Liang and J. Zhou, *Acta Phys.-Chim. Sin.*, 2022, **38**, 2111003.
8 E. Faegh, T. Omasta, M. Hull, S. Ferrin, S. Shrestha, J. Lechman, D. Bolintineanu, M. Zuraw and W. E. Mustain, *J. Electrochem. Soc.*, 2018, **165**, A2528–A2535.
9 G. Yang, Q. Li, K. Ma, C. Hong and C. Wang, *J. Mater. Chem. A*, 2020, **8**, 8084–8095.
10 H. Pan, Y. Shao, P. Yan, Y. Cheng, K. S. Han, Z. Nie, C. Wang, J. Yang, X. Li, P. Bhattacharya, K. T. Mueller and J. Liu, *Nat. Energy*, 2016, **1**, 16039.
11 B. Wu, G. Zhang, M. Yan, T. Xiong, P. He, L. He, X. Xu and L. Mai, *Small*, 2018, **14**, 1703850.
12 Q. Ren, Y. Yuan and S. Wang, *ACS Appl. Mater. Interfaces*, 2022, **14**, 23022–23032.
13 J. Yang, J. Cao, Y. Peng, W. Yang, S. Barg, Z. Liu, I. A. Kinloch, M. A. Bissett and R. A. W. Dryfe, *ChemSusChem*, 2020, **13**, 4103–4110.
14 N. Zhang, F. Cheng, J. Liu, L. Wang, X. Long, X. Liu, F. Li and J. Chen, *Nat. Commun.*, 2017, **8**, 405.
15 Q. Dai, L. Li, B. Hu, Y. Jia, T. Tu, T. K. A. Hoang, M. Zhang and L. Song, *Mater. Today Commun.*, 2022, **31**, 103578.
16 Z. Liu, Y. Yang, B. Lu, S. Liang, H. J. Fan and J. Zhou, *Energy Storage Mater.*, 2022, **52**, 104–110.
17 W. J. Jeon, H. Kim and S. H. Byeon, *Colloids Surf., A*, 2022, **640**, 128416.
18 R. Flouty, E. AbiAad, S. Siffert and A. Aboukaïs, *J. Therm. Anal. Calorim.*, 2003, **73**, 727–734.
19 J. Chen, W. Shi and J. Li, *Catal. Today*, 2011, **175**, 216–222.
20 M. Chang, J. Wu, D. Chen and S. Ye, *Corros. Sci. Technol.*, 2018, **17**, 1–5.
21 L. Gong, R. Tang, Y. Zhu and D. Chen, *Int. J. Miner., Metall. Mater.*, 2012, **19**, 800–804.
22 B. R. Strohmeier and D. M. Hercules, *J. Phys. Chem. C*, 1984, **88**, 4922–4929.
23 Y. Wang, L. Chen, M. Chen, Z. Zhong, Q. Meng and W. Xing, *Sci. China Mater.*, 2019, **62**, 527–535.
24 Y. O. Yesilbag, F. N. Tuzluca and M. Ertugrul, *J. Mater. Sci.: Mater. Electron.*, 2019, **30**, 8201–8209.
25 X. Guo, J. Zhou, C. Bai, X. Li, G. Fang and S. Liang, *Mater. Today Energy*, 2020, **16**, 100396.
26 W. Yang, W. Yang, Y. Huang, C. Xu, L. Dong and X. Peng, *Chin. Chem. Lett.*, 2022, **33**, 4628–4634.
27 Y. Li, P. Wu, W. Zhong, C. Xie, Y. Xie, Q. Zhang, D. Sun, Y. Tang and H. Wang, *Energy Environ. Sci.*, 2021, **14**, 5563–5571.
28 Y. Liu, S. Liu, X. Xie, Z. Li, P. Wang, B. Lu, S. Liang, Y. Tang and J. Zhou, *InfoMat*, 2023, **5**, e12374.
29 Z. Pan, J. Yang, J. Yang, Q. Zhang, H. Zhang, X. Li, Z. Kou, Y. Zhang, H. Chen, C. Yan and J. Wang, *ACS Nano*, 2020, **14**, 842–853.

30 X. Xie, J. Li, Z. Xing, B. Lu, S. Liang and J. Zhou, *Natl. Sci. Rev.*, 2023, **10**, nwac281.
31 Y. Song, P. Ruan, C. Mao, Y. Chang, L. Wang, L. Dai, P. Zhou, B. Lu, J. Zhou and Z. He, *Nano-Micro Lett.*, 2022, **14**, 218.
32 X. Cai, Y. Liu, J. Zha, F. Tan, B. Zhang, W. Yan, J. Zhao, B. Lu, J. Zhou and C. Tan, *Adv. Funct. Mater.*, 2023, 2303009.
33 H. Chen, S. Cai, Y. Wu, W. Wang, M. Xu and S. J. Bao, *Mater. Today Energy*, 2021, **20**, 100646.
34 Z. Shen, Z. Tang, C. Li, L. Luo, J. Pu, Z. Wen, Y. Liu, Y. Ji, J. Xie, L. Wang, Y. Yao and G. Hong, *Adv. Energy Mater.*, 2021, **11**, 2102055.
35 Y. Zeng, X. Zhang, Y. Meng, M. Yu, J. Yi, Y. Wu, X. Lu and Y. Tong, *Adv. Mater.*, 2017, **29**, 1700274.
36 H. Tang, W. Chen, N. Li, Z. Hu, L. Xiao, Y. Xie, L. Xi, L. Ni and Y. Zhu, *Energy Storage Mater.*, 2022, **48**, 335–343.
37 J. Gao, X. Xie, S. Liang, B. Lu and J. Zhou, *Nano-Micro Lett.*, 2021, **13**, 69.
38 J. Yang, G. Yao, Z. Li, Y. Zhang, L. Wei, H. Niu, Q. Chen and F. Zheng, *Small*, 2023, **19**, 2205544.
39 L. C. Dong, Y. B. Zhong, S. Zhe, T. Y. Zheng and H. Wang, *RSC Adv.*, 2016, **6**, 21037–21042.
40 S. Islam, M. H. Alfaruqi, V. Mathew, J. Song, S. Kim, S. Kim, J. Jo, J. P. Baboo, D. T. Pham, D. Y. Putro, Y.-K. Sun and J. Kim, *J. Mater. Chem. A*, 2017, **5**, 23299–23309.